

# Direct numerical simulation of turbulence in a sheared air–water flow with a deformable interface

By M. FULGOSI<sup>1</sup>, D. LAKEHAL<sup>1</sup>†, S. BANERJEE<sup>2</sup>  
AND V. DE ANGELIS<sup>2</sup>

<sup>1</sup>Institute of Energy Technology, Swiss Federal Institute of Technology, ETH-Zentrum/CLT, CH-8092 Zurich, Switzerland

<sup>2</sup>Department of Chemical Engineering, University of California, Santa Barbara, CA 93106, USA

(Received 24 April 2002 and in revised form 12 November 2002)

Direct numerical simulation has been performed to explore the turbulence near a freely deformable interface in a countercurrent air–water flow, at a shear Reynolds number  $Re_* = 171$ . The deformations of the interface fall in the range of capillary waves of wavenumber  $ak = 0.01$ , and very small phase speed-to-friction velocity ratio,  $c/u_*$ . The results for the gas side are compared to open-channel flow data at the same shear Reynolds number, placing emphasis upon the influence of the waves in the interfacial viscosity-affected region, and away from it in the outer core flow. Comparison shows a similarity in the distribution of the turbulence intensities near the interface, confirming that for the range of flow conditions considered, the lighter phase perceives the interface like a flexible solid surface, at least in the limit of non-breaking waves. Overall, in a time-averaged sense, the interfacial motion affects the turbulence in the near-interface region; the most pertinent effect is a general dampening of the turbulent fluctuating field which, in turn, leads to a reduction in the interfacial dissipation. Furthermore, the turbulence is found to be less anisotropic at the interface than at the wall. This is confirmed by the analysis of the pressure–rate-of-strain tensor, where the effect of interfacial motion is shown to decrease the pressure strain correlation in the direction normal to the interface and in the spanwise direction. The analysis of the turbulent kinetic energy and Reynolds stress budgets reveals that the interface deformations mainly affect the so-called boundary term involving the redistribution of energy, i.e. by the action of pressure, turbulent fluctuations and molecular viscosity, and the dissipation terms, leaving the production terms almost unchanged. The non-zero value of the turbulent kinetic energy at the interface, together with the reduced dissipation, implies that the turbulent activity persists near the interface and contributes to accelerating the turbulent transfer mechanisms. Away from the interface, the decomposition of the fluctuating velocity gradient tensor demonstrates that the fluctuating rate-of-strain and rate-of-rotation at the interface influence the flow throughout the boundary layer more vigorously. The study also reveals the streaky structure over the deformable interface to be less organized than over a rigid wall. However, the elongation of the streaks does not seem to be much affected by the interfacial motion. A simple qualitative analysis of the quasi–streamwise vortices using different eduction techniques shows that the interfacial turbulent structures do not change with a change of boundary conditions.

---

† Author to whom correspondence should be addressed: lakehal@iet.mavt.ethz.ch

## 1. Introduction

The fundamental mechanisms controlling heat and mass transfer across gas–liquid interfaces play a central role in the modelling of contacting multi-component systems. Whether the process is purely diffusive, such as soluble gas absorption, or involving condensation-induced suction, the exchange process is generally dominated by interfacial shear and/or turbulence. From a practical viewpoint, the subject is equally important to nuclear and chemical engineering, and to environmental problems. For example, a good understanding of interfacial exchange processes is essential for the thermal hydraulics of the class of nuclear power plants resorting to passive emergency cooling systems. Of primary importance in this case is to understand the behaviour of the steam–air mixtures vented into the containment pools. On a much larger scale, more specifically in marine climatology, quantifying the rate of mass transfer through absorption of carbon dioxide by the oceans is important, as well as the impact of aerosol production and transport from surface wave breaking (Melville 1996). The interest in this field is to relate the transfer mechanisms properly to the imposed interfacial shear, and the way this shear scales with the turbulence structure.

Progress towards a sufficient understanding of the various types of gas–liquid exchanges has been hindered by obvious difficulties with measurements and computer simulations. Turbulence near deformable interfaces separating immiscible phases has received less attention than for wall-bounded flows. Recent developments in measuring technology contributed to advancing knowledge in this field (Jaehne *et al.* 1987; Rashidi & Banerjee 1990; Komori, Nagaosa & Murakami 1993*a*; Kumar, Gupta & Banerjee 1998), but there are still many non-clarified issues regarding the way molecular and turbulent transport processes interact with the transfer mechanisms. This is particularly crucial in the non-wall-bounded flow context, where deformable interfaces are synonymous with surface velocity fluctuations and surface wave generation.

Relating the mass transfer process to the interfacial turbulence structure has been approached mainly via two classes of model, i.e. the *surface renewal theory* (Higbie 1935), and the *eddy diffusivity concept*. For instance, experimental evidence for correlations between the mass transfer rate and the surface renewal motion was demonstrated in most of the experiments dealing with wind-driven turbulence at air–water wavy interfaces (Jaehne *et al.* 1984; Coantic 1986; Komori *et al.* 1993*a*). The presence of interfacial waves was also found to further enhance the exchange processes (Jaehne *et al.* 1987), because part of the energy gained by the waves through the action of the wind is transferred to near-interface turbulence.

The advancement in computer technology and numerical methods has made it possible to investigate flows involving non-flat boundaries using direct numerical simulation (DNS) and large-eddy simulation (LES). For example, Maass & Schumann (1994) resorted to finite-difference DNS to investigate the flow structure over stationary high amplitude-to-wavelength ratio ( $a/\lambda = 0.05$ ) sinusoidal waves, and observed large separation regions downstream of the wave crests. De Angelis, Lombardi & Banerjee (1997) employed pseudo-spectral DNS for the flow over a wavy wall with  $a/\lambda = 0.025$  and  $0.05$ , and reported significant effects of the wavy boundary on the turbulence statistics and the mean flow. Cherukat *et al.* (1998), performing spectral-element DNS of the flow over stationary sinusoidal waves with  $a/\lambda = 0.05$ , confirmed the modification of the mean flow only; the local turbulence appeared to be less influenced when rescaled with the increased (effective) friction velocity.

With their LES study of flow over a wavy wall up to  $a/\lambda = 0.1$ , Henn & Sykes (1999) were able to reproduce most of the flow features observed in moderate high- $Re$  experiments. DNS studies dealing with non-stationary sinusoidal waves are very rare, except for the work of Sullivan, McWilliams & Moeng (2000). Their high-amplitude waves ( $ak = 0.1$ ) were found to significantly influence the mean flow and turbulence characteristics. Moreover, they observed that in comparison to stationary waves, slow moving waves increase the form drag, whereas fast moving waves decrease it.

DNS studies devoted to the analysis of turbulence at interfaces, involving two-phase flows, have been relatively few. Some early important work was presented with regard to the turbulence structure near free surfaces with and without shear (Lam & Banerjee 1992; Komori *et al.* 1993*b*; Lombardi, De Angelis & Banerjee 1996). Because of its relative simplicity, stratified gas–liquid flow has been the best-suited configuration to investigate the underlying physics at the interface. The DNS-based study of Lombardi *et al.* (1996) centred around a flat interface configuration, where gas and liquid were coupled through continuity of velocity and stress jump conditions at the interface. The authors found that turbulence characteristics on the gas side are similar to those at the wall. This led them to conclude that in some two phase flow problems, depending on the density ratio between the phases, the lighter phase might look at the interface like a solid surface. De Angelis (1998) extended the work of Lombardi *et al.* (1996) to non-flat interfaces by considering stratified flow with a freely deformable interface in the capillary wave regime.

Following the work of Lombardi *et al.* (1996) and De Angelis (1998), the present investigation aims at analysing in great detail the interfacial sublayer, with emphasis on the gas side because of the presumed analogy between near-wall and near-interface turbulence. The issue is approached by means of a global analysis of the energy budgets and the interfacial turbulence structure obtained from a rigorous DNS of a sheared air–water flow with a freely deformable interface, within the capillary-wave regime. One objective here is to analyse turbulent flow on the gas side and discuss the wave-induced mechanisms influencing the flow. In fact, the major effect expected from interface deformation in the presence of shear is the extra transverse motion superimposed on the mean flow, and its associated energy, in the direction normal to the interface. The final objective is to exploit the outgoing data to develop suitable near-interface turbulence models useful for practical applications, for example by incorporating them into interface tracking methods, where the topology and dynamics of the interface are directly computed. In contrast to the two-fluid formalism, direct interface tracking algorithms may lead to situations where the interface is perceived like a solid surface to one of the phases, a conjecture to which the employed eddy-diffusivity type of model needs to conform.

The paper is structured as follows: the problem under consideration and the numerical procedure are described in §2. The characteristics of the waves are discussed in §3. The flow statistics are presented in §4, together with the data obtained by repeating the open-channel flow numerical experiment of Lam & Banerjee (1992). In §5, the budgets for the turbulent kinetic energy and for the Reynolds stresses are discussed, and the main differences relative to open-channel flow data are highlighted. The mechanisms behind turbulence interaction with the deformable interface are treated in §6. The flow structure is qualitatively analysed in §7 by use of three different eduction techniques. Finally, conclusions are drawn in §8.

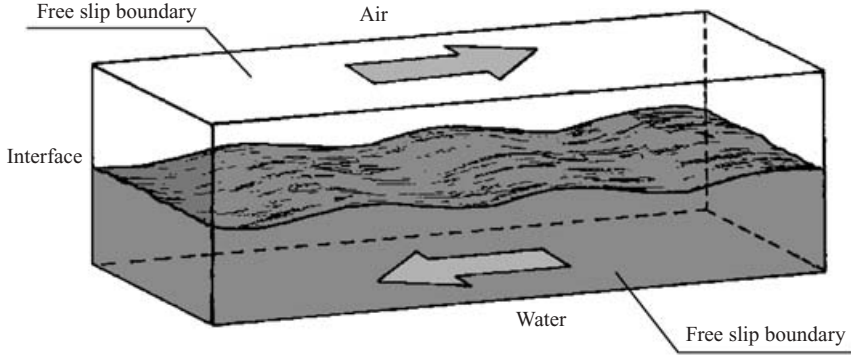


FIGURE 1. Sketch of the simulated problem. The elevation of the waves has been amplified by a factor 5.

**2. Numerical method**

The configuration of the two-phase flow investigated here is sketched in figure 1, where the flow in each subdomain is driven by a constant pressure gradient. The reference quantities used throughout the paper for normalization are the effective shear velocity  $u_*$ , defined by  $u_* = \sqrt{\tau_{int}/\rho}$ , where  $\tau_{int}$  represents the shear stress at the interface, the half-depth of each computational domain  $h$ , and the kinematic viscosity  $\nu$ . It is important to note that at the beginning of the simulation, when the interface is still flat, the interfacial shear balances exactly the imposed mean pressure gradient, so that  $u_*$  corresponds to the shear velocity  $u_\tau$ . As the interfacial waves start to develop, part of the energy is transferred into form drag leading to a reduction of the interfacial shear, i.e.  $u_* < u_\tau$  (see §6.1). The shear-based Reynolds number, defined by  $Re_* = u_* 2h/\nu$ , with  $u_*$  taken at the initial stage of the simulation, is 171 in both phases. Moreover, the non-dimensional time is defined by  $t^+ = t \nu/u_*^2$  in wall units, or by  $t_{ls} = t U_0/h$  in large-scale units, where  $U_0$  is the mean streamwise velocity. With these reference quantities ( $u_*$ ,  $\nu/u_*^2$ ,  $h$ ), the non-dimensional Navier–Stokes equations for the incompressible isothermal Newtonian fluids flowing in the two subdomains are

$$\nabla \cdot \tilde{\mathbf{u}} = 0, \tag{2.1}$$

$$\frac{\partial \tilde{\mathbf{u}}}{\partial t} + \tilde{\mathbf{u}} \cdot \nabla \tilde{\mathbf{u}} = -\nabla \tilde{p} + \frac{1}{Re_*} \nabla^2 \tilde{\mathbf{u}}, \tag{2.2}$$

where  $\tilde{\mathbf{u}}$  is the velocity vector, made non-dimensional by the reference velocity  $u_*$ , and  $\tilde{p}$  is the dynamic pressure normalized by  $\rho u_*^2$ .

In the absence of mass transfer, the gas and liquid phases are explicitly coupled at the interface by the continuity of velocities and shear stresses. The interfacial jump conditions, see for example Delhaye (1974), can be expressed, in non-dimensional form as follows

$$\left. \begin{aligned} &\frac{1}{Re_*} ((\boldsymbol{\tau}_L - \boldsymbol{\tau}_G) \cdot \mathbf{n}) \cdot \mathbf{n} + \tilde{p}_G - \tilde{p}_L + \frac{1}{We} \nabla \cdot \mathbf{n} - \frac{1}{Fr} f = 0, \\ &((\boldsymbol{\tau}_L - \boldsymbol{\tau}_G) \cdot \mathbf{n}) \cdot \mathbf{t}_i = 0, \quad i = 1, 2, \\ &\tilde{\mathbf{u}}_G = \frac{1}{\mathcal{R}} \tilde{\mathbf{u}}_L, \end{aligned} \right\} \tag{2.3}$$

where the subscripts  $L$  and  $G$  stand for liquid and gas respectively,  $\boldsymbol{\tau}$  is the viscous stress tensor,  $f$  measures the vertical displacement of the interface with respect to the

mid-plane,  $\mathbf{n}$  and  $\mathbf{t}_i$  are the normal and the two tangential unit vectors, respectively, and  $\mathcal{R} = \sqrt{\rho_L/\rho_G}$  is the parameter measuring the density ratio. The Weber ( $We$ ) and Froude ( $Fr$ ) numbers are defined as

$$We = \frac{\rho_L h u_{*L}^2}{\sigma}, \quad Fr = \frac{u_{*L}^2 \rho_L}{g h (\rho_L - \rho_G)}, \quad (2.4)$$

where  $\sigma$  stands for the surface tension coefficient. At the outer boundaries, free-slip boundary conditions are employed in order to avoid turbulence generation other than in the interface region. Periodic boundary conditions are applied in the streamwise and spanwise directions.

The interface motion is computed by solving a pure advection equation for the vertical elevation of the interface, denoted here by  $f(\mathbf{x}, t)$ :

$$\frac{\partial f}{\partial t} + \tilde{\mathbf{u}} \cdot \nabla f = 0. \quad (2.5)$$

In contrast to the interface tracking method, this approach, known as the boundary fitting method, cannot be extended to strong topological changes of the interface that might lead to the inclusion of one phase into the other, such as fragmentation and wave breaking (Lakehal, Meier & Fulgosi 2002). For this reason, parameters such as the Weber and Froude numbers were carefully selected. On the basis of scaling arguments, these non-dimensional numbers were set equal to  $We = 4.8 \times 10^{-3}$  and  $Fr = 8.7 \times 10^{-5}$  in order to limit the elevation amplitude and steepness to the range of capillary waves.

At each time step, the distorted physical domain was mapped onto a rectangular parallelepiped on which the Navier–Stokes equations were solved using a pseudospectral technique. Details of the numerical method and the mapping procedure can be found in De Angelis *et al.* (1997). The dimensions of the computational domain are  $4\pi h \times 2\pi h \times 2h$ , with  $h = 0.02$  m. The computational domain for each phase was  $1074 \times 537 \times 171$  wall units in the streamwise, spanwise and normal directions, respectively, with a resolution of  $64 \times 64 \times 65$ , which had been proved satisfactory by Fulgosi *et al.* (2001).

The density ratio between the two phases was such that  $\mathcal{R} = 29.9$ , corresponding to air–water flows at atmospheric pressure and at roughly 320 K. This parameter may be interpreted as an indicator of the degree of dynamic coupling between the phases. In fact, by virtue of the non-dimensional velocity continuity condition

$$\tilde{\mathbf{u}}_G = \frac{1}{\mathcal{R}} \tilde{\mathbf{u}}_L, \quad (2.6)$$

$\mathcal{R}$  can be thought of as a measure indicating the interphase momentum transfer. For example, the limiting case of  $\mathcal{R} \rightarrow \infty$  reduces to a wall-flow-like conjecture, in which case the interphase coupling is minimum. In contrast, the other limiting case of  $\mathcal{R} \rightarrow 1$  reflects a ‘uniform medium’ situation.

### 3. Characteristics of the waves

The topology of the waves developing over a deformable free surface manifests itself in various forms depending on the intensity of the interfacial shear stress caused by the nature of the underlying turbulence. The action of this shear is balanced by two stabilizing factors: one due to gravity and one caused by surface tension (Brocchini & Peregrine 2001).

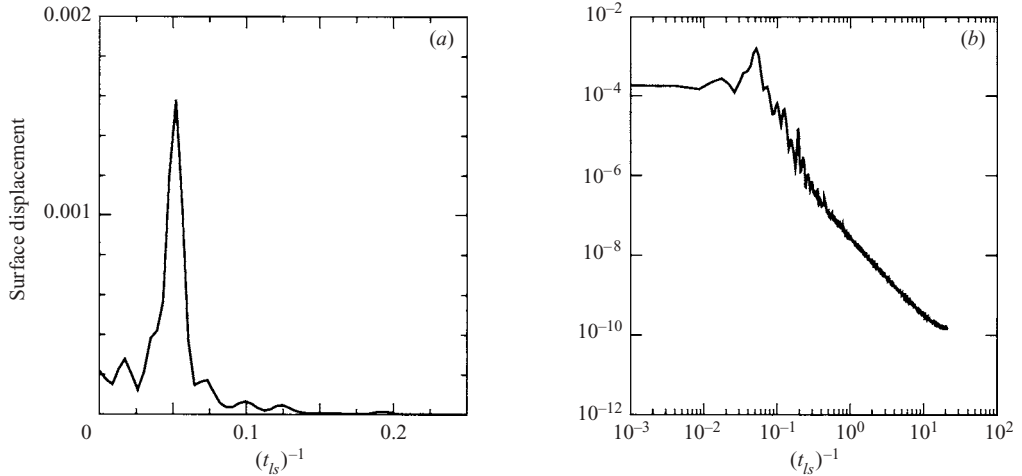


FIGURE 2. Time spectra of the wave amplitude. (a) Linear scale, (b) log–log scale.

In the air–water wave literature, it is customary to characterize the wave motion using the second moments of the joint probability density of the surface displacement  $P(f(\mathbf{x}_1), f(\mathbf{x}_2))$ . In particular, the covariance of the instantaneous non-dimensional surface displacement

$$Z(\mathbf{r}) = \overline{f(\mathbf{x}, t_0)f(\mathbf{x} + \mathbf{r}, t_0)}, \quad (3.1)$$

and the covariance of the non-dimensional surface displacement at a fixed location as a function of time

$$Z(t) = \overline{f(\mathbf{x}, t_0)f(\mathbf{x}, t_0 + t)}. \quad (3.2)$$

The other useful wave-characterizing quantity, defined in terms of the covariance of the surface displacement (3.1), is the two-dimensional wave spectrum

$$\Psi(\mathbf{k}) = (2\pi)^{-2} \int Z(\mathbf{r}) \exp(-i\mathbf{k} \cdot \mathbf{r}) d\mathbf{r}. \quad (3.3)$$

It is important to note that, since the wavenumber  $k$  is here defined in the dimensional space,  $\Psi$  has the dimension of  $[L^2]$ , leading to the following definition of the saturation spectrum of the wave displacement

$$B(\mathbf{k}) = |\mathbf{k}|^2 \Psi(\mathbf{k}). \quad (3.4)$$

See Phillips (1977, 1985) for further exhaustive theoretical details.

The maximum wave amplitude observed in the present simulation was about 0.25 mm, and the maximum waveslope  $ak$  (amplitude  $a$  times wavenumber  $k$ ) never exceeded  $ak = 0.01$ . The time spectra of the non-dimensional wave elevation delivered by the DNS is shown in figure 2. Figure 2(a) is presented in linear scale whereas figure 2(b) is in a log–log scale. The spectrum was obtained over a time interval of  $\Delta t_{ls} = 350$  large-scale non-dimensional time units. The peak value is reached at  $t_{ls} = 20$ , in agreement with the measurements of McCready & Hanratty (1985), and indicates the frequency of the dominating wave. The equilibrium range is well represented in the time spectrum, covering a range of events larger than that of the peak. At the high frequencies, the straight line portion in figure 2(b) indicates that the small-scale dynamical effects induced by the waves cannot be expected to become important since they cannot grow in time. The estimation of the peak frequency

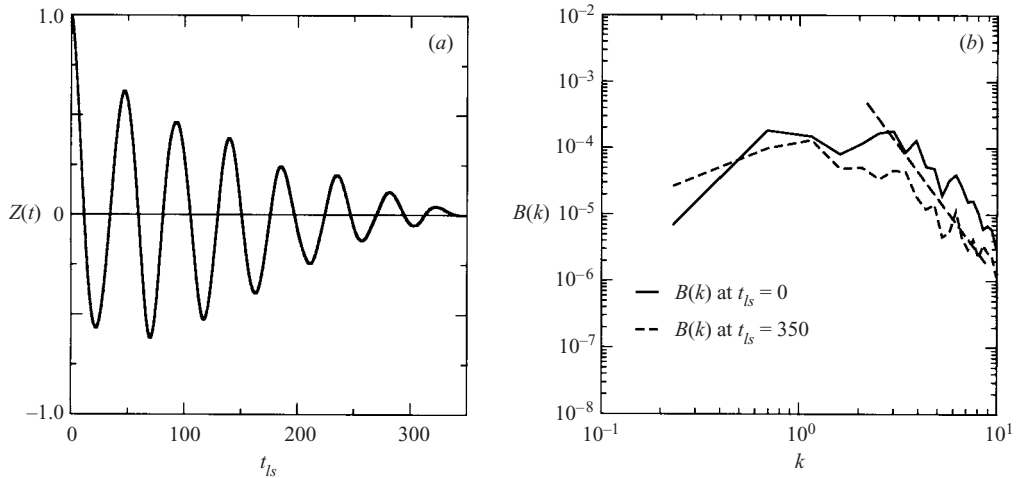


FIGURE 3. (a) Covariance at a fixed point on the interface (autocorrelation) as a function of the non-dimensional time. (b) Saturation spectra at the beginning and the end of the simulation.

has direct implications in modelling the mass transfer coefficient, as postulated by McCready & Hanratty (1985).

The covariance of the surface displacement as a function of time and the saturation spectra of the wave displacement are shown in figures 3(a) and 3(b), respectively. The covariance shows the waves to reach a steady state over the time interval considered in the simulation. In fact, the growth of the waves under the influence of the wind shear cannot continue indefinitely because it is limited by several dissipation effects. In spectral terms, this means that in the wave spectrum there is an upper limit of the spectral density imposed by these dissipation phenomena. The range of wavenumbers over which this occurs is called the saturation range (Phillips 1977). The saturation spectra are plotted in figure 3(b) at two different times during the computation: at the beginning ( $t_{ls} = 0$ ) and at the end ( $t_{ls} = 350$ ) of the time interval over which the statistics were performed. The results clearly show that the waves have not changed their properties in the course of the 350 large-scale time units.

#### 4. Analysis of the turbulent field

As is customary in DNS, statistical analysis of the data was performed by averaging the collected flow database over the two homogeneous directions (i.e.  $(x, y)$ -plane average) and in time. For the type of flow considered here, this procedure can be reliable only if the collected database covers a sufficiently large time interval over which the wave field does not change its properties. In this case, the impact of the interfacial motion can be inferred in an average sense. This applies to the flow over the freely deformable interface since the characteristics of the waves have been shown in §3 to remain invariant in time. After statistically stationary conditions were reached, the flow database was collected over 350 large-scale time units (19 500 time steps) with a frequency of sampling of  $\Delta t_{ls} = 0.04$ , which corresponds roughly to twice the large-eddy turnover time of the flow. The stratified flow data have then been compared to the open-channel flow results obtained by repeating the numerical experiment of Lam & Banerjee (1992). The flow database in this case was collected over 240 large-scale time units (13 500 time steps).

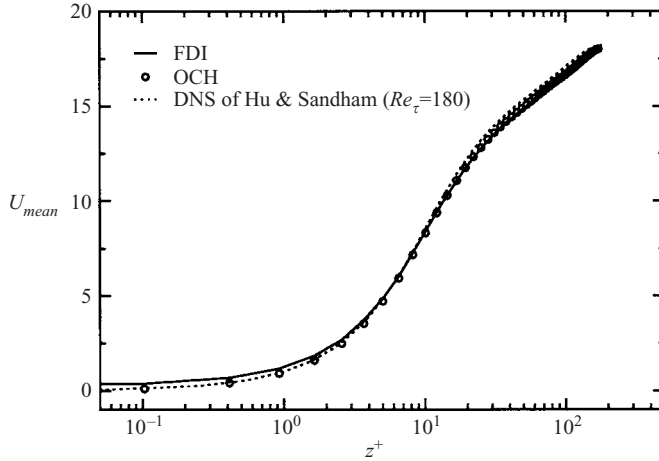


FIGURE 4. Profiles of the mean streamwise velocity.

Because the wave dynamics induces extra motion in the vertical direction of the flow, the velocity field may be thought of as superposition of mean coherent and non-coherent (turbulent) contributions, i.e.

$$\tilde{u}_i = U_i + u_i^w + u_i, \quad (4.1)$$

where  $U_i$  is the mean velocity (i.e. averaged over time and the two horizontal directions),  $u_i^w$  is the flow component induced by the orbital motion, and  $u_i$  is the superimposed turbulent fluctuation. This suggests that, in order to analyse the non-coherent turbulent fluctuating field in stratified flow, it is necessary to separate it from the coherent field,  $u_i^w$ . Also, the wave component is removed in the vertical direction only because the other two components (in the plane tangential to the interface) are negligible, i.e. of the order  $10^{-4}$ . This has been achieved by removing the grid velocity  $u_3^g$  from the vertical velocity component, i.e.  $u_3^w = u_3^g$ , leading to a zero value of  $\tilde{u}_3$  at the interface.

Most of the following results are presented using a logarithmic scale for the abscissa  $z^+ = u_* z / \nu$  in order to appreciate better the changes very close to the interface.

#### 4.1. Velocity field

Figure 4 shows the profiles of the mean streamwise velocity for flow over the deformable interface (referred to as FDI) and for the open channel (OCH). DNS results obtained by Hu & Sandham (2001) for closed-channel flow at  $Re_\tau = 180$  are also included for comparison. The profiles are practically the same starting from  $z^+ = 10$ , but below, while both the wall-bounded flows converge towards zero at the wall, the velocity in the FDI case has a finite value at the interface, corresponding to 2% of the maximum velocity. The root-mean-square (r.m.s) profiles of the velocity fluctuations are presented in figure 5. The behaviour is almost identical, but again, because of different boundary conditions, the r.m.s. values of  $u$  and  $v$  in the FDI case do not start from the same value at the interface/wall. At this stage, the results presented in this section suggest that there is an ‘apparent similarity’ between wall-turbulence and near-interfacial turbulence. In reality, although small in magnitude, differences do exist and manifest themselves in very subtle ways.

The effect of filtering the wave-induced motion from the vertical velocity component has also been investigated, and the results are reported in figure 6, comparing the



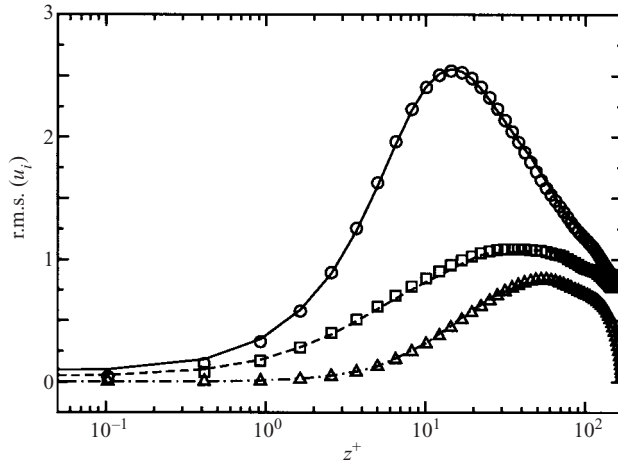


FIGURE 5. Root-mean-square profiles of the three velocity components. Lines and symbols are used to identify FDI and OCH, respectively. — and  $\circ$ , streamwise velocity; --- and  $\square$ , spanwise component; - - - and  $\triangle$ , normal component.

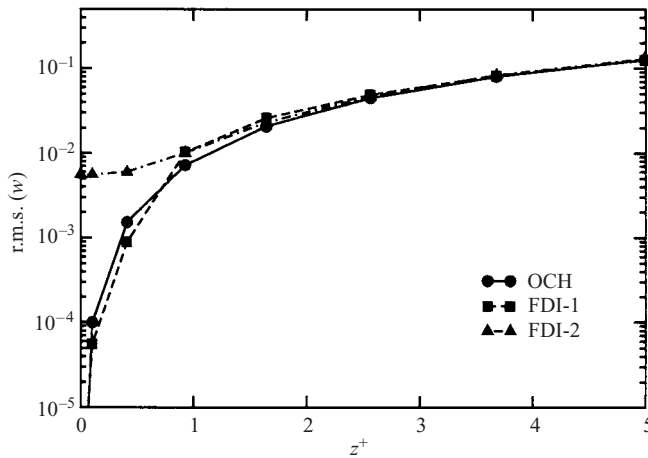


FIGURE 6. Profiles of the r.m.s. of fluctuating vertical velocity near the interface/wall. FDI-1: filtered data ( $\tilde{w} - w^w$ ); FDI-2: unfiltered data ( $\tilde{w}$ ).

r.m.s. of  $\tilde{w} - w^w$  (filtered) to the r.m.s. of  $\tilde{w}$  (unfiltered), referred to as FDI-1 and FDI-2, respectively. The comparison highlights the influence of the wave dynamics on the velocity fluctuating field, although, compared to the maximum value, the r.m.s. of  $\tilde{w}$  is small.

Another persuasive indication that the interfacial deformation acts on the velocity field can be provided by examining the variation of the components of the fluctuating rate-of-strain tensor

$$s_{ij} = \frac{1}{2} \left( \frac{\partial u_i}{\partial x_j} + \frac{\partial u_j}{\partial x_i} \right). \tag{4.2}$$

The analysis, discussed in the context of figure 7, indicates that the most affected components are the off-diagonal ones, i.e.  $s_{12}$ ,  $s_{13}$  and  $s_{23}$ . The lower values of  $s_{13}$  and  $s_{23}$  in the FDI case provide evidence that the impact of the interface dynamics

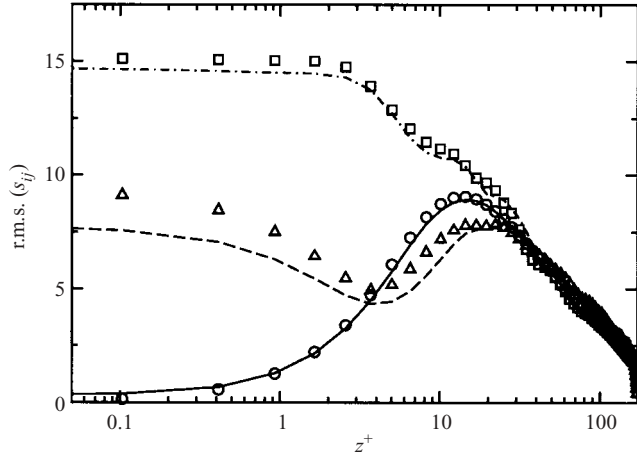


FIGURE 7. Profiles of the r.m.s. of the fluctuating strain tensor  $s_{ij}$ . Lines and symbols are used to identify FDI and OCH, respectively. — and  $\circ$ ,  $s_{12}$ ; --- and  $\square$ ,  $s_{13}$ ; ··· and  $\triangle$ ,  $s_{23}$ .

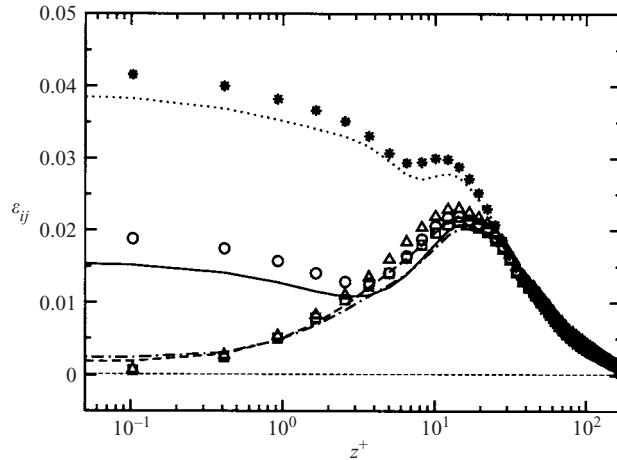


FIGURE 8. Profiles of the off-diagonal components of the dissipation tensor. Lines and symbols are used to identify FDI and OCH, respectively. — and  $\circ$ ,  $\varepsilon_{12}$ ; --- and  $\square$ ,  $\varepsilon_{13}$ ; ··· and  $\triangle$ ,  $\varepsilon_{23}$ ; ··· and  $*$ ,  $\varepsilon$ .

on the turbulence at the interface is to reduce the rate-of-deformation of the fluid in the near-interface region  $z^+ < 12$ . The implications of this result are better measured by looking at the off-diagonal components of the viscous dissipation tensor

$$\varepsilon_{ij} = 2\nu s_{ik}s_{kj} \quad (4.3)$$

plotted in figure 8, together with  $\varepsilon = \varepsilon_{ii}/2$ , the dissipation of the turbulent kinetic energy. The analysis shows that the off-diagonal components of  $\varepsilon_{ij}$  are weakened in the FDI case, in particular  $\varepsilon_{12}$  (because of the significant difference in  $s_{23}$ ); this applies also to  $\varepsilon$ . Thus, it can be concluded that the effect of the interfacial deformations on the near-interfacial turbulence leads to general dampening of the turbulent fluctuating field.

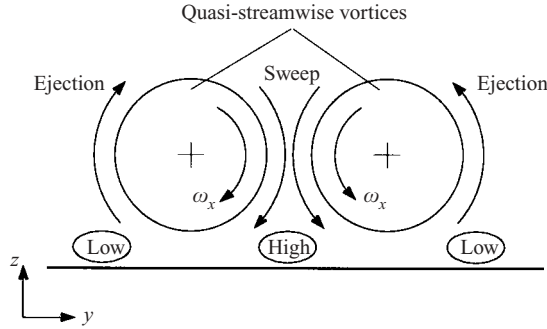


FIGURE 9. Schematic of the interaction between streamwise vorticity  $\omega_x$  and streaky structure.

#### 4.2. Vorticity field

The aim of this section is to evaluate the influence of the interfacial deformations on the flow field away from the interface. Emphasis will be placed upon the modification of the quasi-streamwise vortices. Although the current knowledge on wall-flow structures prompted by DNS is richer than ever, questions regarding certain aspects of the energy transfer and regeneration mechanisms near the wall are still open. The lack of consensus is even more acute as to which of the streamwise velocity streaks or quasi-streamwise vortices are directly implicated in the turbulence self-sustaining mechanisms (Jimenez & Pinelli 1999; Schoppa & Hussain 2002). This latter mechanism, in particular, has long been associated with the dynamics of the quasi-streamwise vortices oriented in the flow direction (Banerjee 1992). Pairs of these quasi-streamwise vortices neighbouring the wall are known to be directly linked to the formation of the streaky structure of the velocity field through two types of event: ejections and sweeps. These two flow events are also known to result from the interaction between the quasi-streamwise vortices (see figure 9). The streaky structure pattern consists of the alternation between regions of low- and high-speed fluid; high-speed regions are associated with low-shear stress regions, and vice versa.

Some preliminary information about the phenomenon of generation of quasi-streamwise vortices has been inferred from the analysis of the fluctuating vorticity field. For instance, it is known that the main contributor to changes of  $\omega_x$  is  $\omega_z(dU/dz)$ , which can be interpreted as the tilting of a vortex with component  $\omega_z$  in the streamwise direction. Figure 10 shows the variation of the r.m.s. of the three components of the vorticity vector for the FDI and OCH cases. Since  $dU/dz$  is almost equal in both configurations, and no substantial differences occur in the variation of  $\omega_z$ , it can be argued that the orientation of the quasi-streamwise vortices is not affected by the interfacial motion, at least in an average sense. Further, the influence of the interfacial deformation on the core flow can also be discussed by examining the behaviour of the fluctuating velocity gradient tensor, decomposed as

$$\frac{\partial u_i}{\partial x_j} = s_{ij} + r_{ij}, \quad (4.4)$$

where  $s_{ij}$  is the fluctuating rate-of-strain tensor (symmetric) defined in (4.2), and  $r_{ij}$  is the fluctuating rate-of-rotation tensor (skew-symmetric), defined as

$$r_{ij} = \frac{1}{2} \left( \frac{\partial u_i}{\partial x_j} - \frac{\partial u_j}{\partial x_i} \right). \quad (4.5)$$

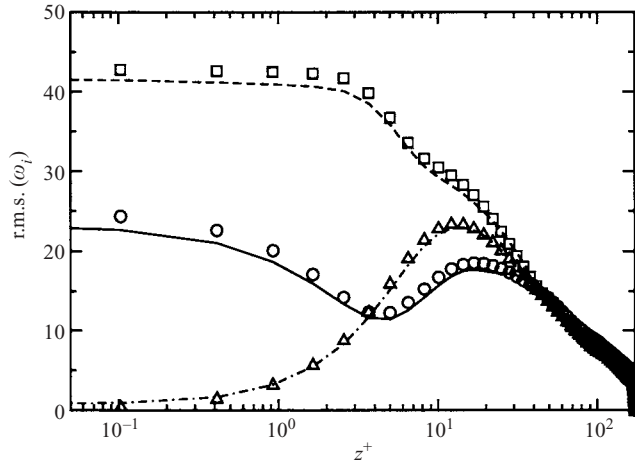


FIGURE 10. Root-mean-square profiles of components of the vorticity vector  $\omega$ . Lines and symbols are used to identify FDI and OCH, respectively. — and  $\circ$ ,  $\omega_x$ ; --- and  $\square$ ,  $\omega_y$ ; -·- and  $\triangle$ ,  $\omega_z$ .

Of particular interest in evaluating the rate-of-deformation/rotation of the fluid, is the second invariant ( $Q$ ) of the velocity gradient tensor, defined as

$$Q = -\frac{1}{2}[tr(\mathbf{r}^2) + tr(\mathbf{s}^2)] = \frac{1}{2}(r_{ij}r_{ij} - s_{ij}s_{ij}). \quad (4.6)$$

Since  $Q$  vanishes at the wall, it cannot be directly used in the present context to estimate the influence on the fluid deformation/strain of the interfacial dynamics. However, useful information can be inferred by analysing separate contributions of  $r_{ij}r_{ij}$  and  $s_{ij}s_{ij}$  in terms of autocorrelation functions between their values at the interface/wall and in the bulk region. The autocorrelation functions have been defined as

$$Corr(r_{ij}) = \frac{\overline{\langle r_{ij}r_{ij} \rangle(0)} \overline{\langle r_{ij}r_{ij} \rangle(z)}}{\langle r_{ij}r_{ij} \rangle^{rms}(0) \langle r_{ij}r_{ij} \rangle^{rms}(z)}, \quad (4.7)$$

$$Corr(s_{ij}) = \frac{\overline{\langle s_{ij}s_{ij} \rangle(0)} \overline{\langle s_{ij}s_{ij} \rangle(z)}}{\langle s_{ij}s_{ij} \rangle^{rms}(0) \langle s_{ij}s_{ij} \rangle^{rms}(z)}, \quad (4.8)$$

where  $\langle r_{ij}r_{ij} \rangle(0)$  stands for the value of the space-averaged ( $x$ - $y$ ) component at the interface/wall, and  $\langle r_{ij}r_{ij} \rangle(z)$  for the values along the direction normal to the interface/wall; the same applies to  $\langle s_{ij}s_{ij} \rangle$ . Figure 11, comparing the autocorrelation functions  $Corr(r_{ij})$  and  $Corr(s_{ij})$ , shows that these are both stronger in the FDI flow configuration than in OCH. A close inspection of the plot reveals that, for the FDI case, the location where the rotation overcomes the strain is 10 wall units earlier than for OCH. This result reflects the fact that the interface affects the evolution of the flow field throughout the entire boundary layer, in contrast to a rigid wall.

#### 4.3. Pressure field

In the vicinity of the wall, pressure fluctuations,  $p$ , ( $z$ ) are a direct measure of the surface excitation force, and are closely linked to flow unsteadiness. The generation of pressure fluctuations in a turbulent boundary layer is coupled to the dynamics of

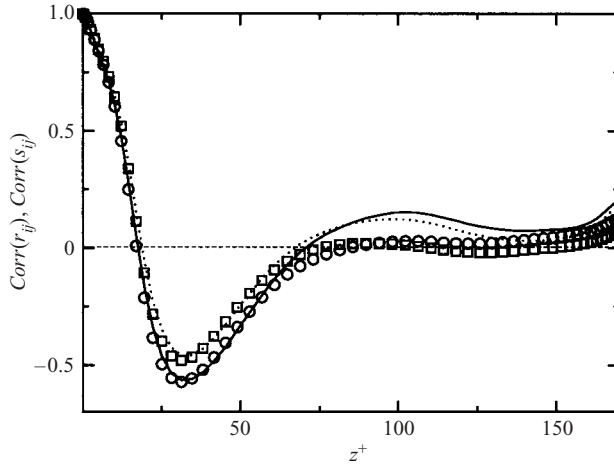


FIGURE 11. Profiles of the autocorrelation function between the  $\langle r_{ij}r_{ij} \rangle$  and  $\langle s_{ij}s_{ij} \rangle$  at the interface/wall and that in the bulk flow. Lines and symbols are used to identify FDI and OCH, respectively. — and  $\circ$ ,  $Corr(r_{ij})$ ;  $\cdots$  and  $\square$ ,  $Corr(s_{ij})$ .

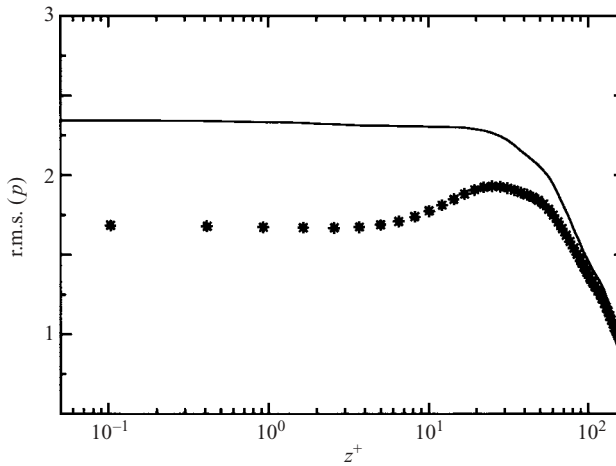


FIGURE 12. Profiles of the r.m.s. pressure fluctuation,  $p$ . Lines and symbols are used to identify FDI and OCH, respectively.

the instantaneous velocity field throughout the entire layer. This coupling is expressed in terms of the following Poisson equation

$$\frac{1}{\rho} \nabla^2 p = -2 \frac{\partial U_i}{\partial x_j} \frac{\partial u_j}{\partial x_i} - \frac{\partial^2}{\partial x_i \partial x_j} (u_i u_j - \overline{u_i u_j}), \tag{4.9}$$

which embodies a dependency on the interaction between the fluctuating velocity field and the mean shear as well as on the nonlinear interaction of the velocity fluctuations with themselves. Moreover, since the instantaneous gradients of the pressure fluctuations are equal to the flux of vorticity from the wall, the wall-pressure fluctuations are intimately related to the vorticity fluctuations and the organization of the turbulent structures within the boundary layer (Robinson 1991). Figure 12 shows the variations in the fluctuating pressure in the direction normal to the interface/wall.

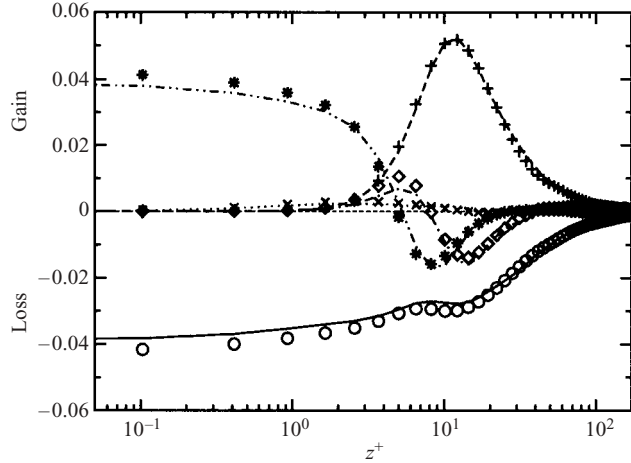


FIGURE 13. Terms in the budget for the TKE in wall units. Lines and symbols are used to identify FDI and OCH, respectively. — and  $\circ$ , dissipation; ---- and +, production;  $\cdots$  and  $\times$ , pressure diffusion; - · - and  $\diamond$ , turbulent diffusion; - · · - and \*, viscous diffusion.

It is readily apparent that the freely deformable interface is associated with a higher level of near-interface pressure fluctuations, which is maintained across the entire viscous sublayer and above ( $z^+ \approx 20$ ). In the OCH case, the r.m.s. of the pressure at the wall is around 1.7, which agrees fairly well with the channel flow data of Kim, Moin & Moser (1987). In the FDI case, the interfacial r.m.s. pressure value is around 2.3, which can be interpreted as resulting from the formation of local pressure gradients promoted by the alternation of ‘hills’ and ‘valleys’ developing over the deformable interface. In § 4.1, it has been shown that the impact of the interfacial motion on the velocity field results in a reduction in the near-interfacial dissipation, via a reduction in the deformations induced by the fluctuating strain,  $s_{ij}$ ; i.e. the fluctuating velocity gradients in the direction normal to the interface are reduced compared to those at the wall. The larger values of the r.m.s. of pressure in the near-interface region are then in accord with the observed dampening of the turbulent fluctuating field; in fact, this is required by conservation of the pressure–rate-of-strain term in equation (5.3).

## 5. Energy budget equations

### 5.1. Turbulent kinetic energy budget

The transport equations for the turbulent kinetic energy (TKE),  $k = (\overline{u^2} + \overline{v^2} + \overline{w^2})/2$ , can be derived from the Navier–Stokes equations. For incompressible turbulent flow, the transport equation is given by

$$\frac{Dk}{Dt} = \underbrace{-\overline{u_i u_j} \frac{\partial U_i}{\partial x_j}}_{\text{Production}} - \underbrace{\frac{1}{\rho} \frac{\partial}{\partial x_i} \overline{p u_i}}_{\text{Press. Diff.}} - \underbrace{\frac{1}{2} \frac{\partial}{\partial x_j} \overline{u_i u_i u_j}}_{\text{Turb. Transp.}} + \underbrace{\frac{1}{2} \nu \frac{\partial^2}{\partial x_j^2} \overline{u_i u_i}}_{\text{Visc. Diff.}} - \underbrace{\nu \frac{\partial u_i}{\partial x_j} \frac{\partial u_i}{\partial x_j}}_{\text{Dissipation}}, \quad (5.1)$$

where  $D/Dt$  is the substantial derivative. The analysis below follows the approach used by Mansour, Kim & Moin (1988). Figure 13 compares the terms on the right-hand side of equation (5.1) for FDI and OCH cases. The only significant difference can be observed close to the interface, where both viscous diffusion and dissipation

rates are smaller in the FDI case. This is due to the previously observed dampening effect of the turbulent field caused by interfacial motion. It is interesting to note that even in the presence of a deformable interface the dissipation rate close to the interface is balanced entirely by the viscous diffusion, exactly as in the case of a rigid wall.

5.2. Reynolds stress budget

The transport equations for the Reynolds stresses are also derived from the Navier–Stokes equations. For incompressible turbulent flow the generic transport equation is given by

$$\begin{aligned} \frac{D}{Dt} \overline{u_i u_j} = & - \underbrace{\left( \overline{u_i u_k} \frac{\partial U_j}{\partial x_k} + \overline{u_j u_k} \frac{\partial U_i}{\partial x_k} \right)}_{\text{Production}} - \frac{1}{\rho} \underbrace{\left( \overline{u_i \frac{\partial p}{\partial x_j}} + \overline{u_j \frac{\partial p}{\partial x_i}} \right)}_{\text{Press. Diff.}} \\ & - \underbrace{\frac{\partial}{\partial x_k} \overline{u_i u_j u_k}}_{\text{Turb. Transp.}} + \nu \underbrace{\frac{\partial^2}{\partial x_k^2} \overline{u_i u_j}}_{\text{Visc. Diff.}} - 2\nu \underbrace{\frac{\partial \overline{u_i}}{\partial x_k} \frac{\partial \overline{u_j}}{\partial x_k}}_{\text{Dissipation}}. \end{aligned} \quad (5.2)$$

It is important to note that the pressure diffusion term provides both a source of energy and a mechanism to redistribute it. This term, also called the velocity–pressure-gradient tensor and denoted by  $\Pi_{ij}$ , can be decomposed into a redistributive part and a transport part as follows

$$\Pi_{ij} = \frac{p}{\rho} \left( \frac{\partial \overline{u_i}}{\partial x_j} + \frac{\partial \overline{u_j}}{\partial x_i} \right) - \frac{\partial}{\partial x_k} \left[ \frac{p}{\rho} (\overline{u_i \delta_{jk}} + \overline{u_j \delta_{ik}}) \right] = \mathcal{R}_{ij} - \frac{\partial}{\partial x_k} \mathcal{T}_{ijk}, \quad (5.3)$$

where  $\delta_{ij}$  indicates the Kronecker delta.  $\mathcal{R}_{ij}$ , the pressure-rate-of-strain tensor, serves to redistribute energy among the Reynolds stresses promoting isotropy of turbulence.  $\mathcal{T}_{ijk}$ , the pressure–transport term, constitutes the source of kinetic energy due to pressure transport. As discussed in §4.3, owing to the homogeneity of the flow in the streamwise and spanwise directions, the transport equation for  $\overline{u_i u_j}$  reduces to  $\Pi_{12} - \varepsilon_{12} = 0$ . The reduction of  $\varepsilon_{12}$  near the interface (see figure 8) is therefore counterbalanced by an increase in  $\Pi_{12}$  through the pressure.

By virtue of continuity, the trace of  $\mathcal{R}_{ij}$  is zero, and consequently this term vanishes in the transport equation of the turbulent kinetic energy (5.1). Each term of the trace of  $\mathcal{R}_{ij}$  is used to define the pressure–strain correlation

$$PS_i = \frac{1}{\rho} p \frac{\partial \overline{u_i}}{\partial x_i}, \quad i = 1, 2, 3. \quad (5.4)$$

A positive value of  $PS_i$  implies a transfer of energy into component  $i$  from the other components, and vice versa.

Figure 14 shows the profiles of the pressure–strain correlation. In both OCH and FDI cases, the streamwise component,  $PS_1$ , transfers energy into the spanwise ( $PS_2$ ) and the normal ( $PS_3$ ) components. What is remarkable is that this effect is less pronounced for FDI, meaning that the streamwise component loses less energy than in the channel flow. Hence, the deformable boundary reduces the interface-normal component less than the solid boundary does. The reduced values of  $PS_2$  and  $PS_3$  occur as  $\mathcal{R}_{22}$  and  $\mathcal{R}_{33}$  are smaller in the flow over a deformable interface than near the wall. This leads to the conclusion that near-interface turbulence is more isotropic than near-wall turbulence.

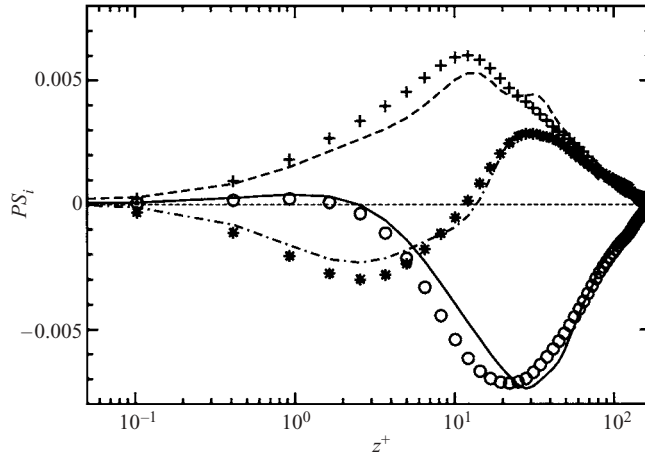


FIGURE 14. Profiles of the pressure–strain correlation. Lines and symbols are used to identify FDI and OCH, respectively. — and  $\circ$ , streamwise direction; ---- and +, spanwise direction; -·- and \*, vertical direction.

The intercomponent energy transfer near a boundary (described by the pressure–strain correlation) can be further explained by considering the presence of two types of effect when the surface is approached: a viscous effect that reduces the turbulence intensities, and a wall-blocking effect that amplifies the tangential turbulence intensities. The latter event is referred to as *splat*; a local region of stagnation flow resulting from impingement on a solid boundary (Perot & Moin 1995). As it cannot penetrate the boundary, the fluid turns and moves parallel to it, yielding a transfer of energy from the normal velocity component to the tangential components and an enhancement of tangential turbulence. The proximity of a vortical structure close to the boundary produces vorticity of opposite sign, which can be ejected away by the primary vortex. This scenario, known as *antisplats*, can be regarded as the counterpart of the *splat* event which explains the energy redistribution between  $PS_i$  components. This clearly shows that interfacial motion weakens the role of splats.

A comparison between the budgets of the normal stress component,  $\overline{uu}$ , is presented in figure 15. In the vicinity of the interface ( $z^+ < 10$ ), turbulent transport, viscous diffusion, and dissipation are smaller in absolute value in FDI than in OCH, while production and pressure diffusion remain unchanged. Close to the interface, the dissipation is entirely balanced by the viscous diffusion. The budgets for  $\overline{vv}$  are presented in figure 16. Again, viscous diffusion, pressure diffusion, and dissipation are smaller in absolute value in FDI than in OCH, whereas turbulent transport remains unchanged. In the spanwise direction there is no production, and close to the interface the dissipation is balanced by viscous diffusion, whereas up to  $z^+ > 10$  the dissipation is entirely balanced by the pressure diffusion term. Figure 17 compares the budgets for the interface/wall normal component  $\overline{ww}$ . In the viscous sublayer no substantial differences can be seen, indicating that the interfacial motion very close to the interface does not affect the balance. However, in the buffer region,  $20 < z^+ < 40$ , pressure diffusion, turbulent transport, and dissipation (the former is not very evident in a logarithmic plot) are more pronounced in FDI than in the OCH case. In the normal direction there is no production either, and the only important source of energy is the pressure diffusion term, which is balanced by turbulent transport and dissipation. A comparison of budgets for the shear stress  $\overline{uw}$ , plotted in figure 18,



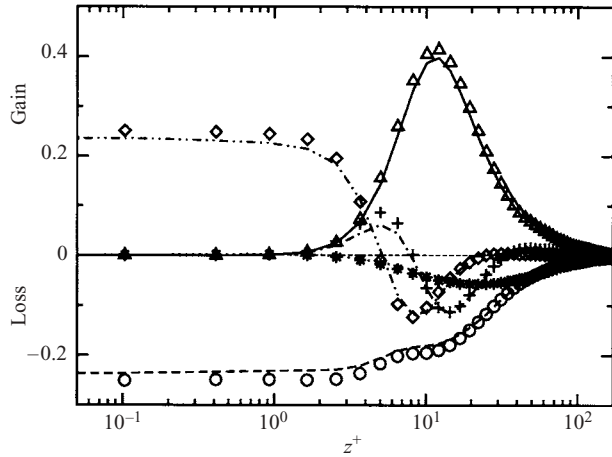


FIGURE 15. Terms in the budget for  $\overline{uu}$  in wall units. Lines and symbols are used to identify FDI and OCH, respectively. — and  $\Delta$ , production; --- and  $\circ$ , dissipation; -·-·- and  $\diamond$ , viscous diffusion; ··· and \*, pressure diffusion; --- and +, turbulent diffusion.

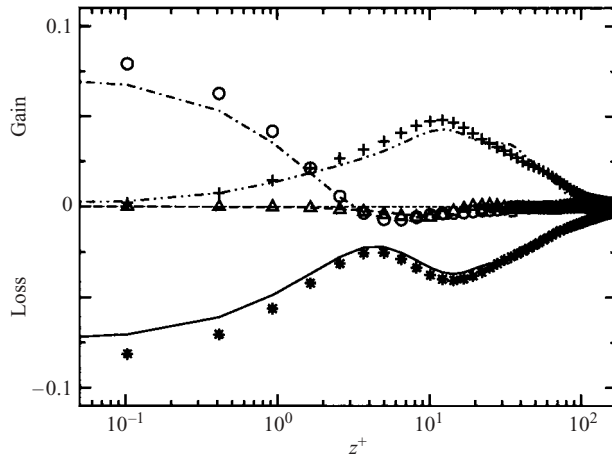


FIGURE 16. Terms in the budget for  $\overline{vv}$  in wall units. Lines and symbols are used to identify FDI and OCH, respectively. — and \*, dissipation; -·-·- and +, pressure diffusion; --- and  $\Delta$ , turbulent diffusion; -·-·- and  $\circ$ , viscous diffusion.

indicates that in both cases the production is balanced by the pressure diffusion term. Viscous diffusion, dissipation, and production remain unchanged in the viscous sublayer, whereas pressure diffusion and turbulent transport are slightly smaller at the deformable interface.

In summary, it can be concluded that the interfacial motion affects the flow in the viscous layer through a reduction of the viscous mechanisms (i.e. dissipation and viscous diffusion) and a reduction of the flux of Reynolds stresses (i.e. turbulent transport). The production mechanisms including pressure diffusion, however, remain unchanged. This confirms the role of the interface deformation in reducing most of the gradients of turbulent correlations (i.e. the terms requiring modelling in equation (5.2)) as the interface is approached.

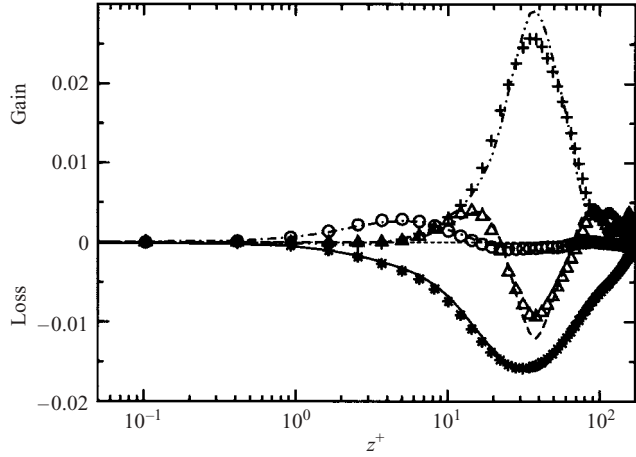


FIGURE 17. Terms in the budget for  $\overline{w\overline{w}}$  in wall units. Lines and symbols are used to identify FDI and OCH, respectively. — and \*, dissipation; -·-·- and +, pressure diffusion; ---- and  $\Delta$ , turbulent diffusion; - - - and  $\bigcirc$ , viscous diffusion.

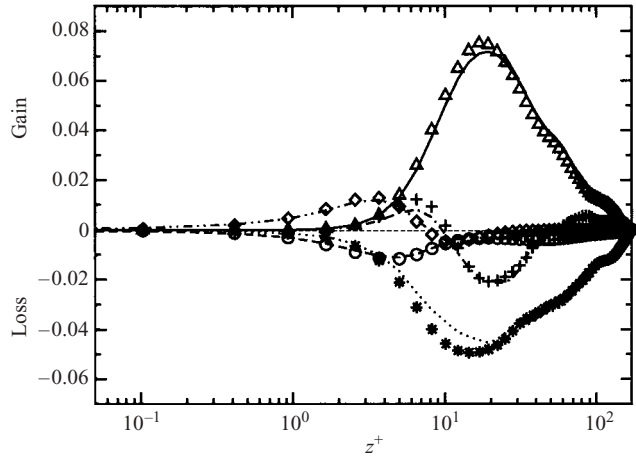


FIGURE 18. Terms in the budget for  $\overline{u\overline{w}}$  in wall units. Lines and symbols are used to identify FDI and OCH, respectively. — and  $\Delta$ , production; - - - and  $\bigcirc$ , dissipation; -·-·- and  $\diamond$ , viscous diffusion; ··· and \*, pressure diffusion; -·-·- and +, turbulent diffusion.

## 6. Turbulence/interface interaction mechanisms

### 6.1. Drag at the sheared deformable interface

Of fundamental interest in turbulent two-phase flow research is a better understanding of the interaction between turbulence and the neighbouring deformable interface. More precisely, identifying the various mechanisms through which interfaces affect turbulence is the key to understanding the subsequent processes of interphase heat and mass transfer, which is the ultimate goal of this work. The turbulence/interface interaction mechanisms induced by the interfacial shear and their relationship to interfacial drag are examined first. The near-interface/wall distributions of the shear stress,  $-\overline{uw}$ , are compared in figure 19. The comparison shows that the peak value is smaller in the two-phase flow, indicating that there is a small drag reduction due

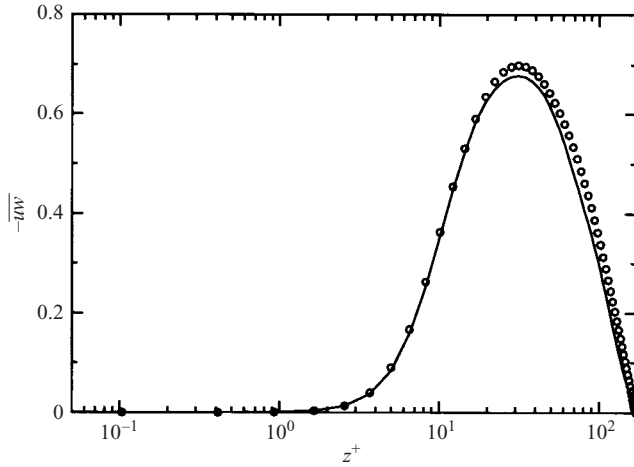


FIGURE 19. Profiles of the shear stress  $-\overline{uw}$ . Lines and symbols are used to identify FDI and OCH, respectively.

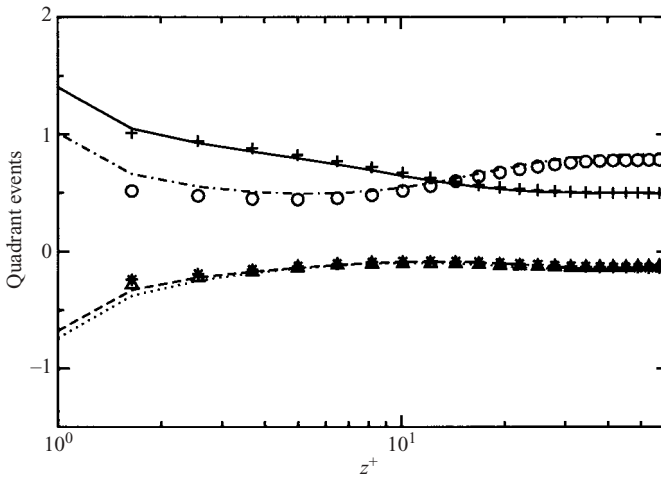


FIGURE 20. Quadrant analysis terms. Lines and symbols are used to identify FDI and OCH, respectively. --- and \*, first quadrant events; — and +, second quadrant events; ··· and  $\Delta$ , third quadrant events; -·- and  $\circ$ , fourth quadrant events.

to interfacial dynamics. This is due to the fact that the form drag, even if very small,  $u_* / u_\tau = 0.986$ , takes energy away from the flow and thus the shear decreases. This result is consistent with the observation that drag reduction can be obtained over adaptive and flexible walls (e.g. compliant coating) rather than rigid walls (Choi 2001). This also suggests that statistically stationary capillary waves may similarly lead to drag reduction, even if by a smaller amount.

A more detailed view of the mechanisms by which the shear stress can be lowered in intensity by interfacial dynamics is provided by the quadrant analysis (Kim *et al.* 1987; Soldati & Banerjee 1998). This analysis quantifies the possible combinations of  $u$  and  $w$  in terms of physical flow events. Figure 20 displays the fractional contribution of each event to the shear stress  $-\overline{uw}$  for both FDI and OCH cases studied. Although first and third quadrant events are favourable to drag reduction, their contribution

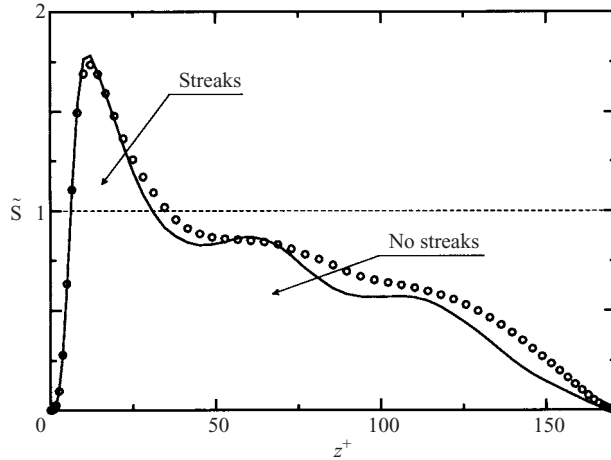


FIGURE 21. Profiles of the nondimensional shear rate parameter. Lines and symbols are used to identify FDI and OCH, respectively.

is actually smaller than the other quadrant events. Sweep events in channel flow are dominant close to the wall, whereas, away, from the wall, ejection events dominate. The crossover point is located at  $z^+ = 12$ . For the FDI case, the variation of quadrant events is small. All the events seem to be enhanced at the interface but the crossover point between the second and fourth quadrant events is still located around  $z^+ = 12$ . Above the crossover point, first and third quadrant events are larger in the FDI case (not clearly noticeable), which explains why the drag reduction is not significant.

### 6.2. Turbulence characteristics

In order to study the flow structure without explicitly employing an identification criterion other than the shear stress, the non-dimensional shear rate parameter  $\tilde{S}$  introduced by Lam & Banerjee (1992) was employed. It is defined by

$$\tilde{S} = \frac{dU}{dz} \frac{|\overline{uw}|}{\varepsilon} = \frac{\mathcal{P}}{\varepsilon} \quad (6.1)$$

and represents the ratio of the rate of production of turbulent kinetic energy  $\mathcal{P}$  to its rate of dissipation  $\varepsilon$ . This parameter is therefore intimately related to the streaky structure of the velocity field, as discussed in §4.2. If  $\tilde{S} > 1$ , the shear is high enough for streaks to form, indicating that the generation of turbulence is more dominant than dissipation. Figure 21 shows a comparison of the time-averaged non-dimensional shear rate parameter,  $\tilde{S}$ , obtained from the DNS of both FDI and OCH flows. In both flow configurations, the formation of the streaks is seen to take place at the same distance from the interface/wall, at  $z^+ \approx 8$ . Figures 22(a) and 22(b) compare two snapshots of the streaky structure (note that, for sake of clarity, the amplitude of the surface elevation has been amplified by a factor of 5). It can be observed that the streaky structure in the channel flow appears to be more regular than on top of the deformable interface. The clear alternation between high- and low-speed regions is also more visible, while overall the streaky pattern looks less organized. However, the streamwise elongation of the streaks does not seem to be affected by the deformation of the interface.

The analysis of the ratio  $\mathcal{P}/\varepsilon$  via local conditions rather than global parameters characterizing the boundary layer, can be further detailed in terms of the same shear

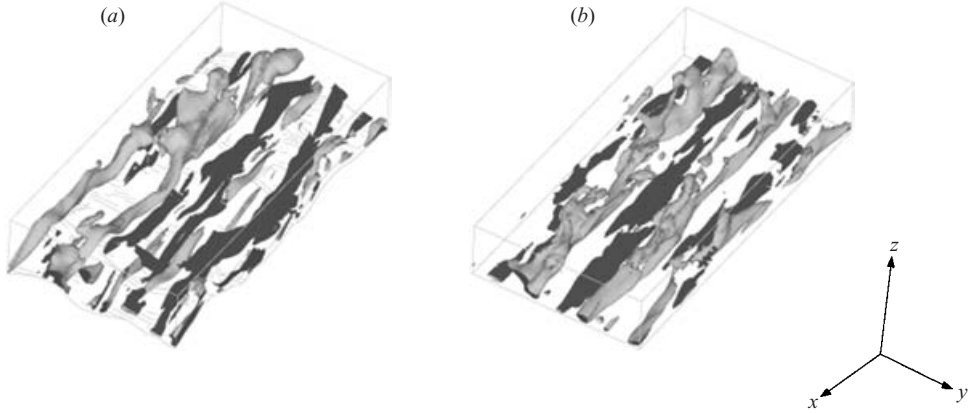


FIGURE 22. Three–dimensional view of the streaky structure in (a) FDI and (b) OCH cases. Light and dark shades indicate low and high speed streaks respectively.

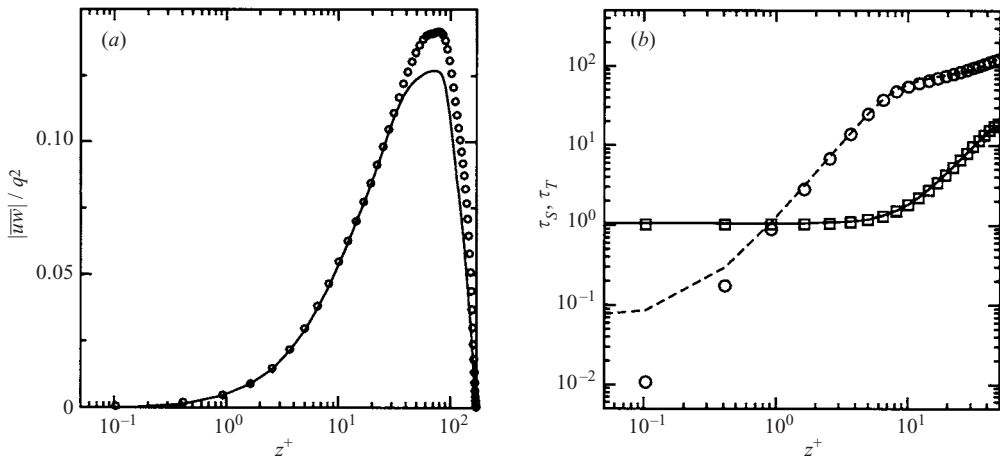


FIGURE 23. (a) Profiles of the structure parameter  $|\overline{uw}|/q^2$ . Lines and symbols are used to identify FDI and OCH, respectively. (b) Time scales. — and  $\square$ ,  $\tau_S$ ; --- and  $\circ$ ,  $\tau_T$ .

rate parameter,

$$\tilde{S} = \frac{\mathcal{P}}{\varepsilon} = S \frac{|\overline{uw}|}{\varepsilon} = \frac{S}{\varepsilon} q^2 \frac{|\overline{uw}|}{q^2} = S^* \frac{|\overline{uw}|}{q^2}, \quad (6.2)$$

where  $S = dU/dz$  and  $q^2 = 2k$ . With this definition the two contributions to  $\mathcal{P}/\varepsilon$ , namely the structure parameter  $|\overline{uw}|/q^2$  and  $S^* = \tau_T/\tau_S$ , the ratio of the turbulent time scale  $\tau_T = l_T/u_T$ , to the time scale characterizing the mechanical deformation,  $\tau_S = (dU/dz)^{-1}$ , can be separated. In the latter definition,  $l_T = q^3/\varepsilon$  stands for the turbulent length scale, and  $u_T = q$  for the corresponding velocity scale. The structure parameter is the ratio of shear to the trace of the turbulent stress tensor, representing the degree of turbulence anisotropy. The previous discussion of the Reynolds stress budget has revealed that the main role of interface motion is to act on the viscous and transport mechanisms, in particular on the pressure–rate-of-strain tensor, promoting the isotropy of near-interface turbulence. Further evidence of this result is provided in the context of figure 23(a), where the peak value of the anisotropy parameter in FDI appears to be lower than in the OCH case. The two time scales defining  $S^*$

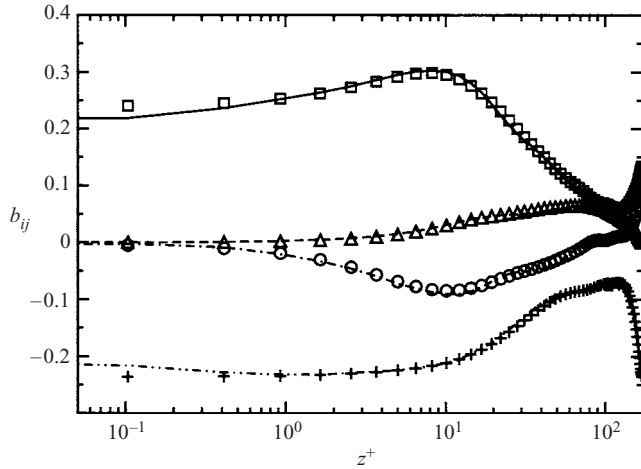


FIGURE 24. Profiles of the components of the anisotropy tensor. Lines and symbols are used to identify FDI and OCH, respectively. — and  $\square$ ,  $b_{11}$ ; --- and  $\triangle$ ,  $b_{13}$ ; -·- and  $\circ$ ,  $b_{22}$ ; ··· and  $+$ ,  $b_{33}$ .

are plotted against  $z^+$  in figure 23(b) both for the FDI and the OCH cases. It can be observed that while  $\tau_S$  is overall of the same magnitude,  $\tau_T$  does not vanish near the interface as it does near the wall, implying that the smallest scales of turbulence remain active approaching the interface whereas they vanish as the wall is approached. Therefore, the role of the interfacial motion also consists in accelerating the turbulent transfer processes.

The degree of turbulence anisotropy can best be obtained by an analysis of the anisotropy tensor, defined as

$$b_{ij} = \frac{\overline{u_i u_j}}{q^2} - \frac{1}{3} \delta_{ij}. \quad (6.3)$$

In contrast to equation (6.2) which compares the magnitude of the shear stress to that of the turbulent kinetic energy, the above relation indicates the magnitude of each stress component to the turbulent kinetic energy. The distribution of the non-zero  $b_{ij}$  components are compared in figure 24. Deviations in the profiles near the interface/wall are visible only for  $b_{11}$  and  $b_{33}$ ; the other two components show no such deviations. In fact, the absolute values of  $b_{11}$  and  $b_{33}$  at the wall are greater than at the deformable interface, which, as discussed above, is expected owing to the imposed near-interface/wall boundary conditions. This, again, confirms that the interfacial motion yields a global dampening of the turbulent fluctuating field in the vicinity of the interface which, in turn, explains why the near-interface turbulence appears less anisotropic than the near-wall one.

## 7. Coherent structure identification

Hussain (1983) defines a coherent structure as a connected, large-scale turbulent fluid mass with a phase-correlated vorticity throughout its spatial extent. The separation between coherent and non-coherent motion is of crucial importance to obtain a better understanding of the transfer processes. In fact, in a turbulent boundary layer, streamwise coherent structures have been linked to ejections and sweeps, which are responsible for draining slow-moving fluid into the outer region and high-momentum

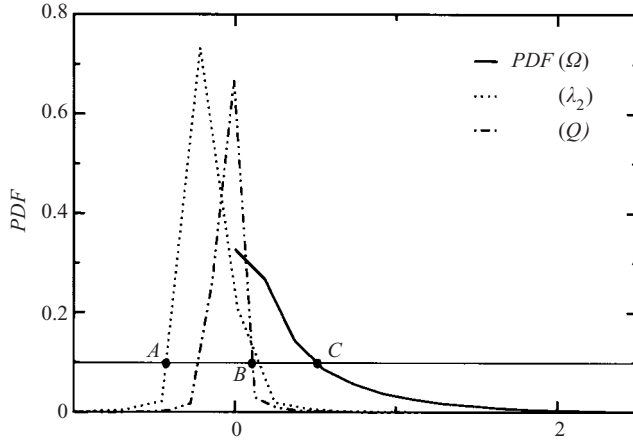


FIGURE 25. PDF distribution of the three different identification criteria.

fluid into the wall region, respectively. These events generate the major part of the drag and are well correlated with heat and mass transfer fluxes (Banerjee 1992). The key issue is to define a suitable criterion that identifies boundaries, topology and dynamics in the spatial and temporal extent of these vortices.

According to Hussain's definition, the high vorticity modulus  $|\omega|$  is a possible candidate for vortex identification in free-shear flow. However, in the presence of a boundary (interface/wall) this criterion fails because the mean shear creates a residual vorticity, which is uncorrelated with the vorticity caused by the coherent motion. Three different vortex identification criteria have therefore been employed here. The first criterion used is the so-called  $Q$ -factor proposed by Hunt, Wray & Moin (1988), which has already been introduced in §4.2.  $Q$  can be thought of as the balance between the rate-of-rotation and the rate-of-strain within the superimposed non-coherent field. Positive values of  $Q$  indicate regions where the strength of rotation overcomes the strain. The second criterion employed is the second largest eigenvalue ( $\lambda_2$ ) of the tensor  $s_{ik}s_{kj} + r_{ik}r_{kj}$ , defined by Jeong *et al.* (1997). With this criterion, coherent vortices are well represented by connected regions where the local value of  $\lambda_2$  becomes negative. The  $\lambda_2 < 0$  and  $Q > 0$  criteria should present very similar types of behaviour, unless the vortices are subjected to high stretching and/or compression. The last identifier used is the streamline rotation vector, proposed by Perry & Chong (1987). The definition of this identifier is based on the classification of complex flow fields by the identification of their three-dimensional critical points. It is defined by

$$\boldsymbol{\Omega} = -\lambda_i \frac{\mathbf{e}_a}{|\mathbf{e}_a|} \frac{\mathbf{e}_a \cdot (\mathbf{r} \times \mathbf{c})}{|\mathbf{e}_a \cdot (\mathbf{r} \times \mathbf{c})|}, \quad (7.1)$$

where  $\lambda_i$  is the imaginary part of the pair of complex eigenvalues of the velocity gradient tensor,  $\mathbf{r}$  is the real part of the conjugate complex eigenvectors corresponding to the complex eigenvalues,  $\mathbf{c}$  is the imaginary part of the conjugate complex eigenvectors and  $\mathbf{e}_a$  is the eigenvector corresponding to the real eigenvalue.

The purpose of this section is to employ these eduction techniques to characterize qualitatively the quasi-streamwise vortices in the turbulent flow over the freely deformable interface, and test their sensitivity to the change in boundary conditions. To compare the results of the different identifiers, isosurface values high enough to capture the strong vortices were selected. For this purpose, the probability density

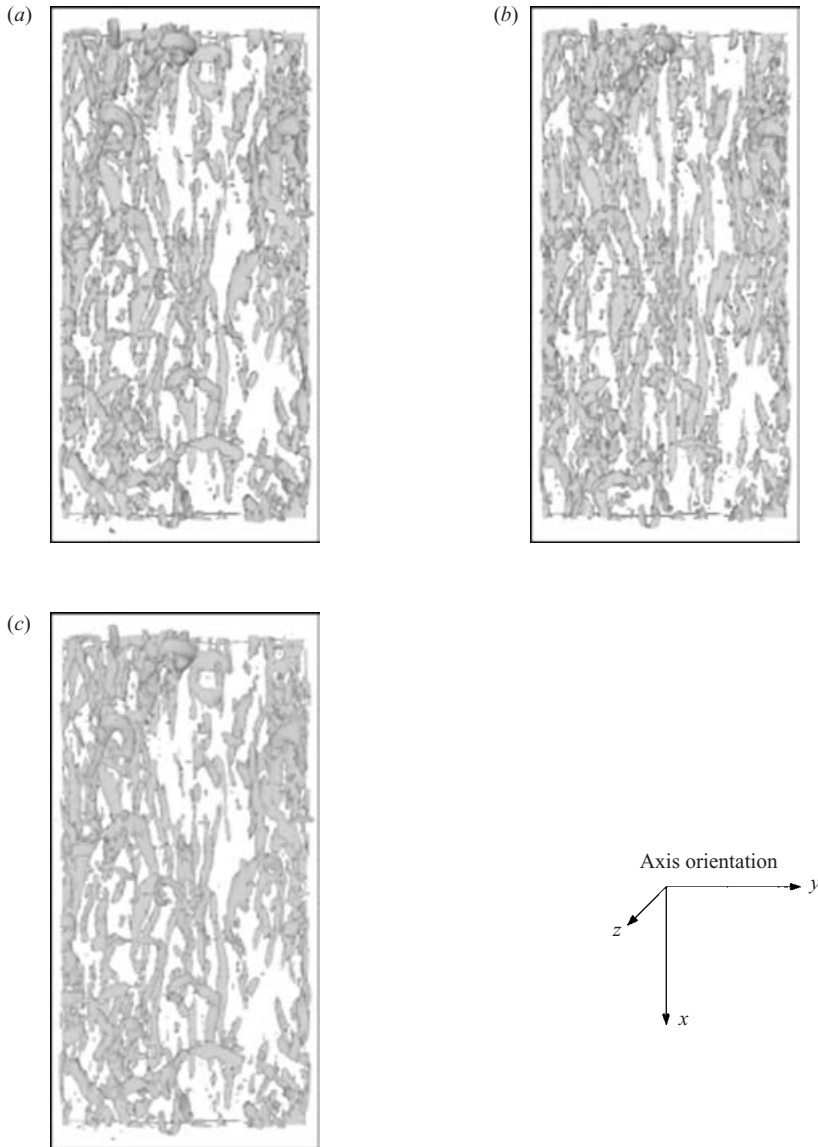


FIGURE 26. Three-dimensional distribution of vortical structures in the FDI case identified by using isosurfaces of (a)  $Q$ , (b)  $-\lambda_2$ , and (c) streamline rotation vector. Values of the isosurfaces were selected with the criterion that  $PDF = 0.1$ .

functions ( $PDF$ ) of the three identifiers were determined and, to make the comparison consistent, isosurface values of  $PDF = 0.1$  were selected, meaning that each identifier carries the same amount of information. The selected isosurface values are identified in figure 25 with  $A$  for the  $Q$ -factor,  $B$  for the  $-\lambda_2$  criterion and  $C$  for the streamline rotation vector, respectively. Figures 26(a), 26(b) and 26(c) display one realization of the instantaneous distributions of the vortical structures in the FDI case by using isosurfaces of  $Q$ ,  $-\lambda_2$  and the streamline rotation vector, respectively. As can be seen, the three different criteria provide virtually the same details of the quasi-streamwise vortices developing over the interface. The comparison between several



flow snapshots of OCH and FDI, using isosurfaces of the streamline rotation vector (result not included here), has not revealed perceptible differences between the wall-bounded and the air water flow. This leads to the conclusion that the turbulence structure is not sensitive to small waveslope ripples. However, a detailed quantitative description of the structures could be better inferred from the data using the method of conditional averaging described in Jeong *et al.* (1997).

## 8. Conclusions

Direct numerical simulation of turbulence in a countercurrent air–water flow configuration separated by a deformable interface has been performed. Attention has been focused on the gas side of the interface because of its similarity to wall-bounded flows. A systematic analysis of the near-interface turbulence has been provided. Turbulence intensities for the flow over an interface free to deform were found to be similar to those of wall-turbulence. The r.m.s. values of the off-diagonal components of the fluctuating rate-of-strain tensor are found to be reduced by the interfacial motion, implying a general dampening of the turbulent fluctuating field near the interface. This effect is manifested by a significant reduction in the magnitude of the off-diagonal components in the dissipation tensor. This result was further corroborated by the increased value of the r.m.s. of the fluctuating pressure. Analysis of the autocorrelation function of the trace of the fluctuating rate-of-strain and rate-of-rotation tensors has shown that the interfacial deformation determines the cross-over point where the rotation overcomes the strain and affects the flow field more deeply into the boundary layer. The differences in the turbulent kinetic energy and Reynolds stress budgets are localized in the dissipation, viscous diffusion and turbulent transport terms in the direction normal to the interface. These terms are seen to be slightly smaller than in wall turbulence, whereas the production contributions remain unchanged. A study of the pressure–strain correlation reveals that although the streamwise component remains the only source of energy, the spanwise and normal components are smaller in absolute value, suggesting that the near-interface turbulence is less anisotropic than that near the wall. This conclusion is further confirmed by examining the anisotropy parameter and anisotropy tensor. However, quadrant analysis applied to the shear stress does not reveal important differences in the fractional contributions of individual events compared to wall-turbulence. A detailed study of the non-dimensional shear rate parameter shows that the turbulent kinetic energy at the interface does not vanish, suggesting that the turbulent transfer mechanisms are enhanced by the interfacial motion. The streaky structure of the flow over the deformable interface was seen to be somewhat less organized than at the wall. Three well-known eduction techniques, namely isosurfaces of  $Q$ ,  $-\lambda_2$  and the streamline rotation vector, are used to identify the structure of the turbulent flow. A simple qualitative comparison leads to the conclusion that the quasi-streamwise vortices are not significantly modified by the presence of the freely deformable boundary. The small differences found between near-wall and near-interface turbulence might be due to the relatively small value of the Reynolds number, and to the fact that the numerical algorithm is not able to handle strong deformation of the interface. However, these findings provide the starting point for further investigations that use large-eddy simulation coupled with level set methods, which are capable of exploring large-Reynolds-number situations featuring wave breaking.

The authors would like to thank Professor George Yadigaroglu for his valuable contribution to this work, and the anonymous reviewers for providing useful comments on the earlier version of the paper. The co-authors from UC-SB acknowledge support for the development of the computer program from the US Department of Energy, contract number DE-FG03-85ER13314 and NASA, contract number NAG3-2414. All computations were performed on the NEC SX-5 at the Swiss Center for Scientific Computing (CSCS) in Manno, Switzerland.

## REFERENCES

- BANERJEE, S. 1992 Turbulence structures. *Chem. Engng Sci.* **47**, 1793.
- BROCCHINI, M. & PEREGRINE, D. H. 2001 The dynamics of strong turbulence at the free surface. Part 1. Description. *J. Fluid Mech.* **449**, 225.
- CHERUKAT, P., NA, Y., HANRATTY, T. J. & McLAUGHLIN, J. B. 1998 Direct numerical simulation of a fully developed turbulent flow over a wavy wall. *Theoret. Comput. Fluid Dyn.* **11**, 109.
- CHOI, K. 2001 Turbulent drag-reduction mechanisms: strategies for turbulent management. *Turbulence Structure and Modulation* (ed. A. Soldati & R. Monti). CISM Courses and Lectures, vol. 415 p. 161.
- COANTIC, M. 1986 A model of gas transfer across air–water interfaces with capillary waves. *J. Geophys. Res.* **91**, 3925.
- DE ANGELIS, V. 1998 Numerical investigation and modeling of mass transfer processes at shared gas–liquid interface. PhD Thesis, UCSB.
- DE ANGELIS, V., LOMBARDI, P. & BANERJEE, S. 1997 Direct numerical simulation of turbulent flow over a wavy wall. *Phys. Fluids* **9**, 2429.
- DELHAYE, J. M. 1974 Jump conditions and entropy sources in two-phase systems. Local instant formulation. *Intl J. Multiphase Flow* **1**, 305.
- FULGOSI, M., LAKEHAL, D., BANERJEE, S. & YADIGAROGLU, G. 2001 Direct numerical simulation of turbulence and interfacial dynamics in counter-current air–water flows. *Proc. of DLES-4, in Direct and Large-Eddy Simulation – IV* (ed. B. J. Geurts, R. Friedrich & O. Metais). ERCOFTAC Series, vol. 8. Kluwer.
- HENN, D. S. & SYKES, R. I. 1999 Large-eddy simulation of flow over wavy surfaces. *J. Fluid Mech.* **383**, 75.
- HIGBIE, R. 1935 The rate of absorption of a pure gas into a still liquid during short periods of exposure. *Trans. AIChE* **31**, 365.
- HU, Z. & SANDHAM, N. D. 2001 Large-domain simulation of Couette and Poiseuille flow. *Proc. 2nd Intl Symp. on Turbulent and Shear Flow Phenomena* (ed. E. Lindborg, A. Johansson, J. Eaton et al.). KTH, Stockholm, Sweden.
- HUNT, J. C. R., WRAY, A. A. & MOIN, P. 1988 Eddies, stream and convergence zones in turbulent flows. *Rep. CTR-588*, Center For Turbulence Research.
- HUSSAIN, A. K. M. F. 1983 Coherent structures – reality and myth. *Phys. Fluids* **26**, 2816.
- JAEHNE, B., HUBER, W., DUTZI, A., WAIS, T. & IMBERGER, J. 1984 Wind–wave-tunnel experiments on the Schmidt number and wave field dependence of air–water gas exchange. *Gas Transfer at Water Surfaces* (ed. W. Brutsaert & G. H. Jirka). Reidel/North Holland.
- JAEHNE, B., MUENNICH, O., BOESINGER, R., DUTZI, A., HUBER, W. & LIBNER, P. 1987 On the parameters influencing air–water gas exchange. *J. Geophys. Res.* **92(C2)**, 1937.
- JEONG, J., HUSSAIN, F., SCHOPPA, W. & KIM, J. 1997 Coherent structures near the wall in a turbulent channel flow. *J. Fluid Mech.* **332**, 185.
- JIMENEZ, J. & PINELLI, A. 1999 The autonomous cycle of near-wall turbulence. *J. Fluid Mech.* **389**, 335.
- KIM, J., MOIN, P. & MOSER, R. 1987 Turbulence statistics in fully developed channel flow at low Reynolds number. *J. Fluid Mech.* **177**, 133.
- KOMORI, S., NAGAOSA, R. & MURAKAMI, Y. 1993a Turbulence structure and mass transfer across a sheared air–water interface in wind-driven turbulence. *J. Fluid Mech.* **249**, 161.
- KOMORI, S., NAGAOSA, R., MURAKAMI, Y., CHIBA, S., ISHII, K. & KUWAHARA, K. 1993b Direct numerical simulation of three-dimensional open-channel flow with zero-shear gas–liquid interface. *Phys. Fluids A* **5**, 115.

- KUMAR, S., GUPTA, R. & BANERJEE, S. 1998 An experimental investigation of the characteristics of free-surface turbulence in channel flow. *Phys. Fluids* **10**, 437.
- LAKEHAL, D., MEIER, M. & FULGOSI, M. 2002 Interface tracking towards the direct simulation of heat and mass transfer in multiphase flows. *Intl J. Heat Fluid Flow* **23**, 242.
- LAM, K. & BANERJEE, S. 1992 On the condition of streaks formation in a bounded turbulent flow. *Phys. Fluids A* **4**, 306.
- LOMBARDI, P., DE ANGELIS, V. & BANERJEE, S. 1996 Direct numerical simulation of near-interface turbulence in coupled gas–liquid flow. *Phys. Fluids* **8**, 1643.
- MAASS, C. & SCHUMANN, U. 1994 Numerical simulation of turbulent flow over a wavy boundary. *Proc. of DLES-1, in Direct and Large-Eddy Simulation – I* (ed. P. R. Voke, L. Kleiser & J. P. Chollet). ERCOFTAC Series, Vol. 26. Kluwer.
- MANSOUR, N. N., KIM, J. & MOIN, P. 1988 Reynolds-stress and dissipation-rate budgets in a turbulent channel flow. *J. Fluid Mech.* **194**, 15.
- MCCREADY, M. J. & HANRATTY, T. J. 1985 Effect of air shear on gas absorption by a liquid film. *AIChE J.* **31**, 2066.
- MELVILLE, W. K. 1996 The role of surface-wave breaking in air–sea interaction. *Annu. Rev. Fluid Mech.* **28**, 279.
- PEROT, B. & MOIN, P. 1995 Shear-free turbulent boundary layers. Part 1. Physical insight into near-wall turbulence. *J. Fluid Mech.* **295**, 199.
- PERRY, A. E. & CHONG, M. S. 1987 A description of eddying motions and flow patterns using critical point concepts. *Annu. Rev. Fluid Mech.* **19**, 125.
- PHILLIPS, O. M. 1977 *The Dynamics of the Upper Ocean*. Cambridge University Press.
- PHILLIPS, O. M. 1985 Spectral and statistical properties of the equilibrium range in wind-generated gravity waves. *J. Fluid Mech.* **156**, 505.
- RASHIDI, M. & BANERJEE, S. 1990 The effect of boundary conditions and shear rate on streak formation and breakdown in turbulent channel flow. *Phys. Fluids A* **2**, 1827.
- ROBINSON, S. K. 1991 Coherent motion in the turbulent boundary layer. *Annu. Rev. Fluid Mech.* **23**, 601.
- SCHOPPA, W. & HUSSAIN, F. 2002 Coherent structure generation in near-wall turbulence. *J. Fluid Mech.* **453**, 57.
- SOLDATI, A. & BANERJEE, S. 1998 Turbulence modification by large-scale organized electrohydrodynamic flows. *Phys. Fluids* **10**, 1742.
- SULLIVAN, P. P., MCWILLIAMS, J. C. & MOENG, C. H. 2000 Simulation of turbulent flow over idealized water waves. *J. Fluid Mech.* **404**, 47.